

Komatiites reveal a hydrous Archaean deep-mantle reservoir

Alexander V. Sobolev^{1,2}, Evgeny V. Asafov², Andrey A. Gurenko³, Nicholas T. Arndt¹, Valentina G. Batanova^{1,2}, Maxim V. Portnyagin^{2,4}, Dieter Garbe-Schönberg⁵ & Stepan P. Krashennikov²

Archaean komatiites (ultramafic lavas) result from melting under extreme conditions of the Earth's mantle. Their chemical compositions evoke very high eruption temperatures, up to 1,600 degrees Celsius, which suggests even higher temperatures in their mantle source^{1,2}. This message is clouded, however, by uncertainty about the water content in komatiite magmas. One school of thought holds that komatiites were essentially dry and originated in mantle plumes^{3–6} while another argues that these magmas contained several per cent water, which drastically reduced their eruption temperature and links them to subduction processes^{7–9}. Here we report measurements of the content of water and other volatile components, and of major and trace elements in melt inclusions in exceptionally magnesian olivine (up to 94.5 mole per cent forsterite). This information provides direct estimates of the composition and crystallization temperature of the parental melts of Archaean komatiites. We show that the parental melt for 2.7-billion-year-old komatiites from the Abitibi greenstone belt in Canada contained 30 per cent magnesium oxide and 0.6 per cent water by weight, and was depleted in highly incompatible elements. This melt began to crystallize at around 1,530 degrees Celsius at shallow depth and under reducing conditions, and it evolved via fractional crystallization of olivine, accompanied by minor crustal assimilation. As its major- and trace-element composition and low oxygen fugacities are inconsistent with a subduction setting, we propose that its high H₂O/Ce ratio (over 6,000) resulted from entrainment into the komatiite source of hydrous material from the mantle transition zone¹⁰. These results confirm a plume origin for komatiites and high Archaean mantle temperatures, and evoke a hydrous reservoir in the deep mantle early in Earth's history.

We investigated samples of 2.7-billion-year-old komatiites from two well-studied parts of the Abitibi greenstone belt in Canada: Pyke Hill in Munro Township^{11–13} and the Alexo flow¹¹. Using electron probe, ion probe and laser ablation inductively coupled plasma mass spectrometry (LA-ICP-MS), we measured concentrations of water, chlorine, fluorine, carbon, boron and sulfur, boron isotopic composition, as well as contents of a full spectrum of major and trace elements in melt inclusions and major and trace elements in their host olivines. We also analysed by electron probe the compositions of spinel and coexisting skeletal olivine. These data were used to constrain the evolution of melt compositions and the crystallization temperatures of magnesian olivine (forsterite (Fo) 94.5–86.7 mol%). In addition, these data were used to reconstruct the parental melt composition and determine the origin of the komatiite magmas.

Crystallization temperatures were obtained using three different geothermometers: Fe/Mg partitioning between olivine and melt, Sc/Y partitioning between olivine and melt, and Al partitioning between olivine and spinel (see Methods). The resultant temperatures are plotted against Fo content in Fig. 1a and compared with calculated temperatures of komatiite melt containing 0–2 wt% water. For the same

Fo contents of olivine the temperatures from different thermometers agree within the uncertainties. The same thermometers give much lower temperatures when applied to low-Ca boninites (high-Si, high-Mg lavas from subduction settings) from Cape Vogel in Papua New Guinea, for which H₂O in the melt exceeds 2 wt%¹⁴. This demonstrates the capacity of the geothermometers to estimate the crystallization temperatures of hydrous melts. The important conclusion is that the komatiite melts contained small amounts of water.

We measured directly the water and CO₂ contents in melt inclusions using secondary ion mass spectrometry (SIMS). Figure 1b shows that the measured water contents compare well with those inferred from the difference in temperature between anhydrous melt and temperatures obtained from the geothermometers. The measured concentrations of CO₂ in the melt inclusions, corrected for CO₂ contents in vapour bubbles, yield crystallization pressures of 150–250 bar of CO₂-rich fluid (see Methods).

The data indicate gradually decreasing crystallization temperatures with decreasing Fo content of olivine. The most magnesian olivine studied for melt inclusions (Fo 94.5 mol%) started to crystallize at pressures of 150–250 bar and temperatures of around 1,500 °C. Crystallization proceeded until the temperature reached 1,350 °C, when the olivine composition reached Fo 86.7 mol%. The crystallization was accompanied by a gradual decrease of H₂O content in the melt, from around 0.6 ± 0.1 wt% (all errors are 2σ) to almost 0 wt% (Fig. 1a and b). Also, the variations of measured H₂O contents in the inclusions in highly magnesian olivine of Pyke Hill komatiite tend to correlate with the inclusion size, with the lowest values in inclusions with diameters < 30 μm (Supplementary Tables 1–3). We attribute this to degassing that accompanied crystallization at shallow depth or during eruption, and, possibly, to the subsequent diffusional loss of H through the host olivine¹⁵. The H₂O content in inclusions with diameters of 30 μm and larger is constant within analytical error and we consider it to be that of the trapped melt because it also matches, within error, the H₂O content expected from the temperature estimated by Sc/Y partitioning (Extended Data Table 1). A relatively high average CO₂ concentration (168 ± 62 parts per million, p.p.m.) and CO₂/H₂O ratio (0.025 ± 0.005) in these inclusions (Extended Data Table 1) suggests saturation with CO₂-rich (molar CO₂/H₂O = 2.7 ± 0.2) fluid at pressures of 193 ± 69 bar (Methods). Thus, substantial H₂O degassing from the melts at higher pressures, both during and before crystallization of the most Mg-rich olivine, is unlikely, and the estimated H₂O concentrations are considered to be those of the parental melt.

Oxygen fugacity during olivine crystallization was estimated from V partitioning between olivine and melt and from the Sc/V ratio in the melt (see Methods). The two estimates match and correspond to the quartz–fayalite–magnetite buffer minus one log unit for the primary melt. It gradually increases with decreasing forsterite content of olivine (Fig. 2), indicating crystallization of olivine in the system closed for oxygen.

¹Université Grenoble Alpes, Institute Science de la Terre (ISTerre), CNRS, F-38041 Grenoble, France. ²Vernadsky Institute of Geochemistry and Analytical Chemistry, Russian Academy of Sciences, 19 ul. Kosygina, Moscow 119991, Russia. ³Centre de Recherches Pétrographiques et Géochimiques (CRPG), UMR 7358, Université de Lorraine, 54501 Vandœuvre-lès-Nancy, France.

⁴GEOMAR Helmholtz Centre for Ocean Research Kiel, Wischhofstrasse 1-3, 24148 Kiel, Germany. ⁵CAU Kiel University, Institute of Geosciences, Ludewig-Meyn-Strasse 10, 24118 Kiel, Germany.

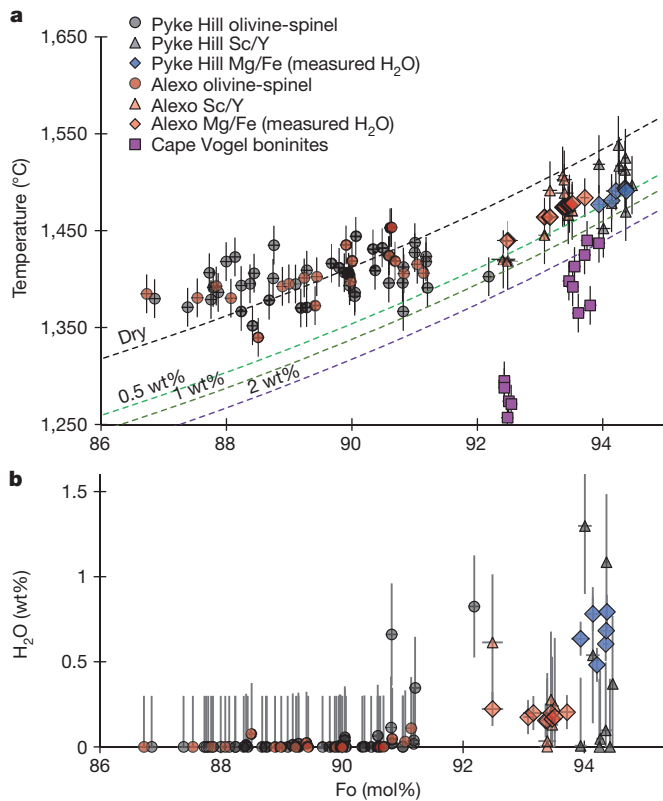


Figure 1 | Crystallization temperatures and H₂O contents in melt versus olivine composition of Abitibi komatiites. **a**, Temperature and model H₂O content versus olivine composition. Temperatures are estimated from Sc/Y olivine–melt, Mg–Fe olivine–melt and Al olivine–spinel geothermometers (see Methods). Dashed lines represent the temperature–composition relationship of olivine in the primary melt of Abitibi komatiites¹¹ at 400 bar and with 0 wt%, 0.5 wt%, 1 wt% and 2 wt% initial H₂O content, calculated using models^{20,30}. Temperatures for Cape Vogel boninites are calculated using the Al olivine–spinel geothermometer (see Methods). The error bars correspond to the reported errors of the thermometers: ± 30 °C for Sc/Y and Al and ± 20 °C for Fe/Mg partitioning. The errors in Fo contents are less than 300 p.p.m. and thus are within symbol sizes. **b**, Measured and calculated H₂O concentrations in melt versus olivine composition. H₂O contents are measured by SIMS (diamonds) or inferred from the difference between the temperatures calculated for ‘dry’ conditions using model³⁰ and those obtained from Sc/Al olivine–melt and Al olivine–spinel geothermometers (see Methods). The errors in measured H₂O contents are within 20% relative to the concentration. The errors in calculated H₂O contents (better than 0.4 wt%) are higher and relate to the errors of temperature calculation (see above). The compositions and calculated temperatures are reported only for inclusions with diameter equal to or larger than 30 μm . As in the text, all errors on figures are 2σ .

The reconstructed melt compositions (see Methods) contain 28–23 wt% MgO (Fig. 2). All Alexo samples have higher contents of Al₂O₃ (not shown), TiO₂, K₂O, La, Ba, Sr, Cl, F and other highly incompatible elements than do Pyke Hill samples, and the less magnesian melts contain higher-than-expected contents of these elements. We attribute these differences to contamination of depleted parental komatiite melt by crustal material with high contents of these elements, as suggested by ref. 16. Further clues to the nature of the contaminant come from the spider diagram (Fig. 3a) and Extended Data Table 1. Melt inclusions in more Fo-rich olivines—samples M810 from Pyke Hill and M823 from Alexo—are moderately depleted in most incompatible elements. Melt inclusions in a more evolved olivine from sample M823 (823-8-ol31) have a flat pattern with slight deficits of Nb (high Ba/Nb = 52) and Ti, and enrichment of Cl, Ba, Sr and Rb. This pattern can be modelled by the assimilation of about 10% of sulfidic

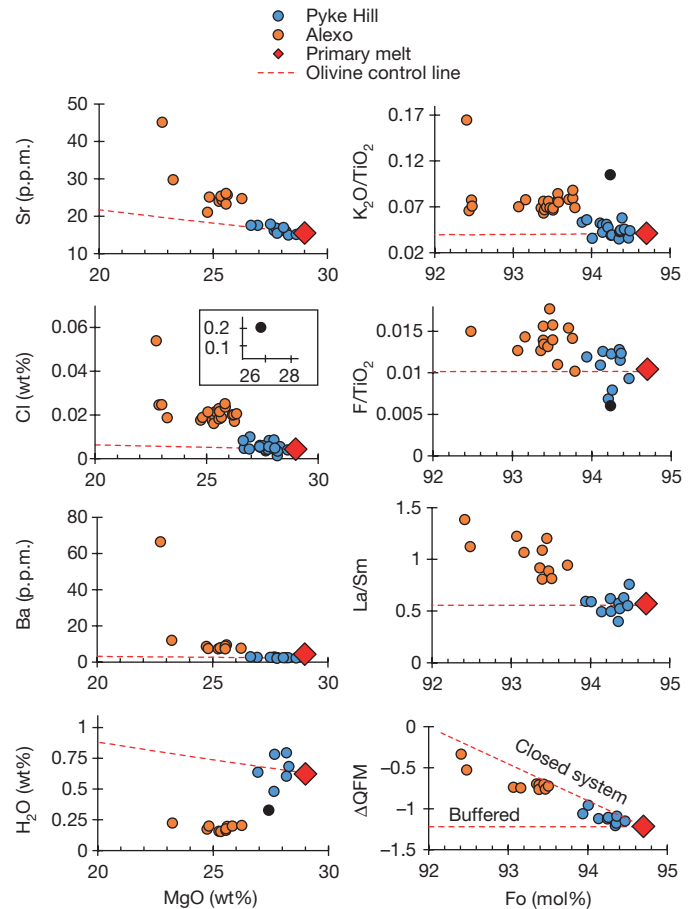


Figure 2 | Compositions and oxygen fugacity of komatiite melt and coexisting olivine. The compositions of melt do not follow the olivine control line, indicating that fractional crystallization of olivine is accompanied by assimilation of rock enriched in highly incompatible elements. Water contents vary in the opposite manner: the highest concentrations are found in the least contaminated parental melts. One extremely chlorine-rich Pyke Hill inclusion, 810-7-ol3, is indicated by a solid black symbol (inset). The compositions are reported only for inclusions with diameter equal to or larger than 30 μm except for inclusion 810-7-ol3, which has diameter 20 μm (see Extended Data Table 1). ΔQFM is the oxygen fugacity compared to the quartz–fayalite–magnetite buffer, estimated using the partition of V between olivine and melt (see Methods).

sediment of the type interlayered with the Alexo komatiites¹⁶. The high Cl and F contents in the evolved melts are also attributed to this contamination (Fig. 2).

To estimate the composition of uncontaminated parental melt of the Abitibi komatiites, we averaged the compositions of melt inclusions hosted by the most magnesian olivine (Fo > 94) of the Pyke Hill samples (Extended Data Table 1). For trace elements more incompatible than Nd, this composition is slightly more depleted than the parental Alexo komatiite, as calculated by ref. 11, but similar to Pyke Hill komatiites¹³.

As shown on Fig. 3b and already noted for melt inclusions in less magnesian olivine (Fo 91–93 mol%), from Zimbabwe komatiites⁶, the trace-element patterns of the parental melt of Abitibi komatiites do not show the features characteristic of subduction related magmas—they lack the negative anomalies of high-field-strength elements (Nb, Zr, Ti), the positive anomalies of large-ion lithophile elements (Rb, Ba, K, Sr), B and Pb, and the U-shaped patterns typical of boninites. In addition, our data show that komatiites crystallized at highly reducing conditions uncharacteristic of supra-subduction magmatism¹⁷. They do, however, show marked enrichment in Cl and possibly in F, but mostly in H₂O. The high Cl content might be partly explained by contamination by

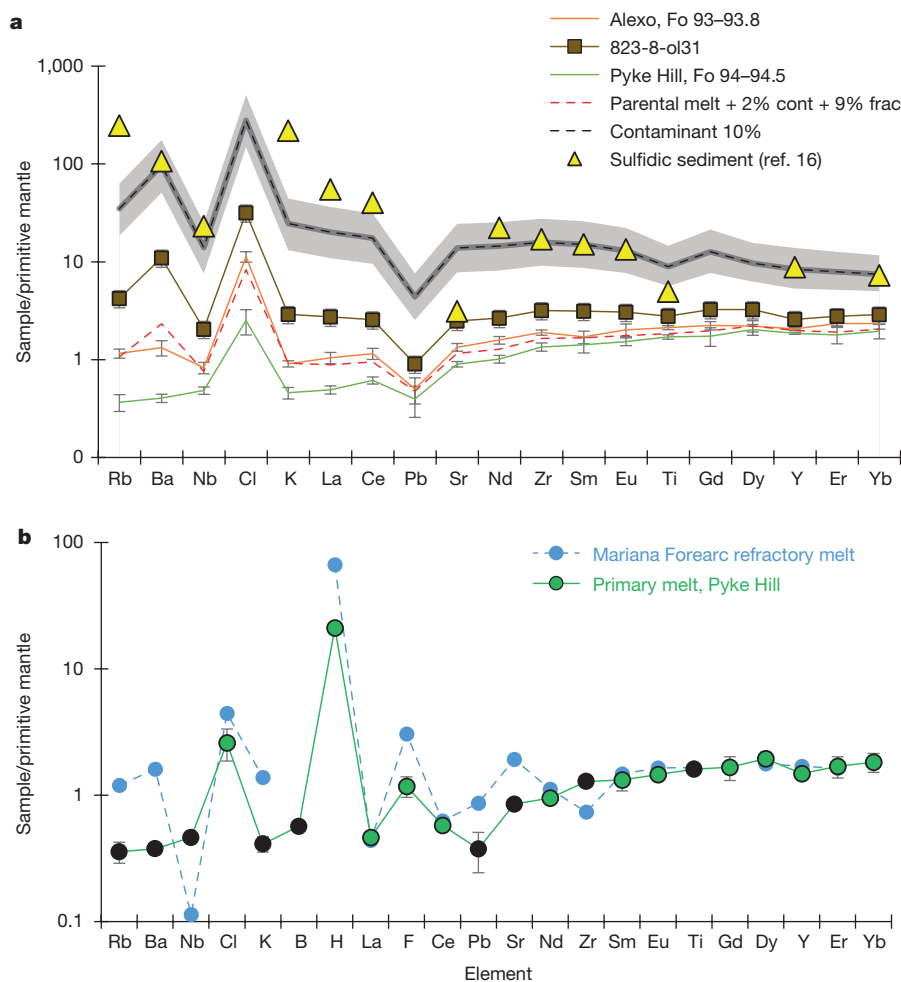


Figure 3 | Incompatible element compositions of primary and evolved melts. a, Spider diagram presenting the compositions of least-contaminated, average, and most-contaminated melt inclusions in olivine from Abitibi komatiites. The composition of the contaminant (see Extended Data Table 1) has been estimated assuming that the most contaminated melt inclusion (823-8-ol31) contains 10% of this contaminant (grey dashed line; see Methods). The grey field illustrates 5%–15% assimilation. These compositions fit reasonably well with the immobile element contents of sulfidic sediment of the type interlayered with the Alexo komatiites¹⁶. The average composition of melt inclusions

Cl-rich brine with high Cl/K₂O and Cl/H₂O ratios, similar to that reported for modern submarine eruptions¹⁸. Direct evidence for the presence of such a component is provided by the composition of inclusion 810-7-ol3 in a highly magnesian Pyke Hill olivine (Fo 94.2 mol%) which has Cl/K₂O = 7, Cl/F = 100 and Cl/H₂O = 0.6 (see Extended Data Table 1 and Fig. 2). Such contamination cannot, however, explain the elevated water and fluorine contents in the parental melt because of its extremely high H₂O/Cl (>160) and its elevated F/Cl (>1). Both ratios are much higher than in the contaminant.

Selected melt inclusions were analysed for boron concentrations and isotopic compositions (see Methods). The uncontaminated melt in a high-Fo olivine of Pyke Hill sample M810 (inclusion 810-6-ol20) has low B concentration (0.23 ± 0.02 p.p.m.) and mantle-like isotope composition ($\delta^{11}\text{B} = -12.9 \pm 10.6\text{‰}$)¹⁹. By contrast, typical moderately contaminated melt trapped in high-Fo olivines from Alexo flow sample M823 (inclusion 823-6-ol16-a) has twice the B concentration (0.46 ± 0.04 p.p.m.) and a heavier B isotope ratio ($\delta^{11}\text{B} = -3.8 \pm 6.8\text{‰}$), probably indicating contamination by a component altered by sea water¹⁹.

The composition of the primary melt of the Abitibi komatiites can be reconstructed from the composition of the uncontaminated parental

in olivine from the Alexo flow (sample M823) is explained by 2% contamination (cont) and 9% of fractional crystallization of olivine (frac) of the least-contaminated melt with such a component. **b**, Spider diagram of primary melt composition compared with refractory subduction-related melt from the Mariana forearc³¹ associated with high-Mg olivine–Fo 93–94 mol%. The positive Rb, Ba and Sr anomalies and negative Nb, Zr and Ti anomalies of the subduction-related melt are absent in the komatiite melt (these elements are indicated by black circles). All elements are normalized to the composition of primitive mantle³². The error bars correspond to 2 σ of the average or analytical error ±20%.

melt by adding equilibrium olivine until equilibrium is reached with Fo 94.7, the most magnesian olivine known in the Abitibi komatiites. To be conservative, we used two different models of Fe/Mg partitioning between olivine and melt^{20,21} (Extended Data Table 1). The overall correction is less than 7 wt% of added olivine. The primary melt contains 30.2 ± 0.5 wt% MgO and is depleted in highly incompatible elements, but contains 0.6 ± 0.1 wt% H₂O and has a very high H₂O/Ce ratio of over 6,000 (Extended Data Table 1). For a pressure of 250 bar, its liquidus temperature is close to 1,530 °C ± 20 °C, about 60 °C lower than the temperature of anhydrous komatiite liquidus. Assuming that the composition of the melt has not changed since its last equilibrium with the source peridotite, we can estimate the potential temperature of the mantle source. We used Herzberg and Asimow's relationship²² between the potential mantle temperature and the low-pressure liquidus temperature and the MgO content of primary melt. Considering its H₂O content (0.6 ± 0.1 wt%) we obtained a potential temperature of 1,730 ± 50 °C. This value exceeds average estimates of the potential temperature for the Archaean non-arc basalts²³ and maximum estimates for Phanerozoic plumes²⁴ by at least 100 °C. This is consistent with a plume origin of Abitibi komatiites⁶ and a higher overall mantle temperature in the Archaean²³.

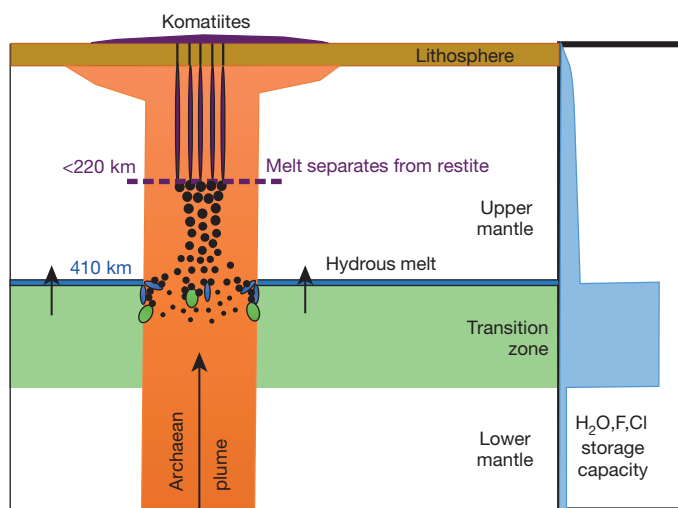


Figure 4 | Cartoon illustrating a hot Archaean plume passing through the mantle transition zone at 410–660 km depth. The plume (orange) traverses the transition zone, which contains excess H_2O , F and Cl in ringwoodite and/or wadsleyite. The plume is partially molten near the top of the transition zone (small black dots) and entrains hydrous melt (blue shapes) either from the layer at the upper boundary of the transition zone or from the hot boundary between the plume and the transition zone. Alternatively or additionally the plume may entrain solid wadsleyite from the transition zone (green shapes). All these hydrous materials introduce H_2O and possibly F and Cl into the plume and accelerate its melting (larger black dots). Further ascent of the plume generates more melt during decompression (large black dots), which then separates from the source (restite is the solid residue after melting of peridotite) and ascends to the surface without reaction with peridotite (purple stripes). The maximum separation depth has been estimated from the composition of the primary melt and the experimental data for maximum pressure of generation of a melt containing 30 wt% MgO without equilibrium with garnet³³.

The source of H_2O in the primary komatiite melt must have had high ratios of H_2O to the most incompatible elements such as the light rare-earth elements (LREE), Nb, K, Rb, Ba, Pb and B. The ratios of mobile to immobile trace elements and the isotope composition of B should be similar to those in the mantle.

In the crust, a possible source of H_2O could be ultramafic rocks altered by seawater (serpentinites) or brines. Saturated brines have high concentrations of NaCl and would produce $\text{H}_2\text{O}/\text{Cl}$ ratios in contaminated melts of 8–50 (ref. 18), values that are far lower than those in the reconstructed komatiite parental melt ($\text{H}_2\text{O}/\text{Cl} > 160$). Serpentinites contain 10–15 wt% H_2O and thus around 5 wt% of their assimilation could yield the elevated H_2O contents of the parental komatiite melt. However, this, and any other source produced by seawater alteration, lacks the mantle ratios of mobile to immobile elements, as well as a mantle-like boron isotope ratio¹⁹ and low B concentration. In addition, the assimilation of serpentinite alone—that is, without other crustal rocks with high incompatible element contents such as basalt or sediment—is improbable.

An alternative explanation—the hydration of originally dry melt inclusions by volume diffusion of H_2O through the host olivine¹⁵—is inconsistent with the relatively low crystallization temperatures estimated for magnesian olivines, which indicate the presence of H_2O in the parental melt (Fig. 1 and Extended Data Table 1). We thus consider a crustal source of the H_2O in the parental komatiite melt unlikely.

Mantle sources of Phanerozoic intraplate magmas (including apparent plumes) and mid-ocean-ridge basalts do not have high $\text{H}_2\text{O}/\text{Ce}$ ratios²⁵. Their maximum values (400) are more than 15 times lower than those we estimated for the primary komatiite melt (>6,000). One alternative source might be a fluid released by dehydration of subducting slabs in supra-subduction settings⁸, but such a source is inconsistent

with the trace-element composition (Fig. 3b) and low oxygen fugacity of the komatiite melts.

Another possible source is the mantle transition zone at 410–660 km depth. Experimental studies have shown that the high-pressure polymorphs of olivine—wadsleyite and ringwoodite—can accommodate high contents of H_2O and halogens compared to other incompatible elements^{10,26,27}. Accordingly, the transitional zone peridotite could have exceptionally high ratios of H_2O , F, (and possibly Cl) to LREE, Nb, K, Rb, B and Ba. The recent finding of H_2O -rich ringwoodite in diamond²⁸ provides evidence that transition-zone peridotite indeed contains at least 1 wt% of H_2O . We thus consider the transition zone as a likely source of H_2O and a possible source of halogens in the primary melt of the Abitibi komatiites.

We envisage two mechanisms whereby water could be transferred from the transition-zone peridotite to the source of komatiite (Fig. 4). In the first, the transformation of wadsleyite to olivine-bearing peridotite at the top of the transition zone and/or on the hot boundary of a plume produces hydrous melt¹⁰ with high H_2O to LREE, Nb, K, Rb, B and Ba ratios similar to that of the initial bulk rock. Entrainment of a few per cent of such hydrous melt would accelerate partial melting by decompression within the rising plume, which would then produce primary komatiite melt. An alternative mechanism is entrainment of solid water-bearing ringwoodite or wadsleyite into the plume as it traverses the transition zone. Both scenarios require that hydrous mantle was already present 2.7 billion years ago. This implies either that subduction started very early in the Earth history and delivered enough water to the transition zone by 2.7 billion years ago, or that H_2O originally became concentrated in the deep Earth mantle during accretion²⁹. The elevated contents of Cl and F relative to other incompatible elements in the komatiite parental melt (Fig. 3b) could also originate from the transition zone²⁷.

Why do Phanerozoic plumes not have excess H_2O (ref. 25), if they too pass through the transition zone? One explanation would be that the plume source of Archaean komatiites was so hot that, when it traversed the transition zone, it contained partial melt that took in water from ringwoodite or wadsleyite, whereas Phanerozoic plumes were completely solid at these depths. In such a scenario, the transition-zone water filter¹⁰ acts for the superhot Archaean plumes in the opposite direction to that of present-day mantle upwelling.

Online Content Methods, along with any additional Extended Data display items and Source Data, are available in the online version of the paper; references unique to these sections appear only in the online paper.

Received 28 October 2015; accepted 19 January 2016.

1. Herzberg, C. Depth and degree of melting of komatiites. *J. Geophys. Res. Solid Earth* **97**, 4521–4540 (1992).
2. Nisbet, E. G., Cheadle, M. J., Arndt, N. T. & Bickle, M. J. Constraining the potential temperature of the Archaean mantle—a review of the evidence from komatiites. *Lithos* **30**, 291–307 (1993).
3. Arndt, N. *et al.* Were komatiites wet? *Geology* **26**, 739–742 (1998).
4. Campbell, I. H., Griffiths, R. W. & Hill, R. I. Melting in an Archaean mantle plume—heads it's basalts, tails it's komatiites. *Nature* **339**, 697–699 (1989).
5. Herzberg, C. *et al.* Temperatures in ambient mantle and plumes: constraints from basalts, picrites, and komatiites. *Geochem. Geophys. Geosyst.* **8**, Q02006 (2007).
6. McDonough, W. F. & Ireland, T. R. Intraplate origin of komatiites inferred from trace-elements in glass inclusions. *Nature* **365**, 432–434 (1993).
7. Allègre, C. J. in *Komatiites* (eds Arndt, N. T. & Nisbet, E. G.) 495–500 (George Allen and Unwin, 1982).
8. Grove, T. L. & Parman, S. W. Thermal evolution of the Earth as recorded by komatiites. *Earth Planet. Sci. Lett.* **219**, 173–187 (2004).
9. Parman, S. W., Grove, T. L., Dann, J. C. & de Wit, M. J. A subduction origin for komatiites and cratonic lithospheric mantle. *S. Afr. J. Geol.* **107**, 107–118 (2004).
10. Bercovici, D. & Karato, S. Whole-mantle convection and the transition-zone water filter. *Nature* **425**, 39–44 (2003).
11. Lahaye, Y. & Arndt, N. Alteration of a komatiite flow from Alexo, Ontario, Canada. *J. Petrol.* **37**, 1261–1284 (1996).
12. Pyke, D. R., Naldrett, A. J. & Eckstrand, O. R. Archaean ultramafic flows in Munro township, Ontario. *Geol. Soc. Am. Bull.* **84**, 955–977 (1973).
13. Puchtel, I. S., Walker, R. J., Brandon, A. D. & Nisbet, E. G. Pt-Re-Os and Sm-Nd isotope and HSE and REE systematics of the 2.7 Ga Bellingwue and Abitibi komatiites. *Geochim. Cosmochim. Acta* **73**, 6367–6389 (2009).

14. Kamenetsky, V. S., Sobolev, A. V., Eggins, S. M., Crawford, A. J. & Arculus, R. J. Olivine-enriched melt inclusions in chromites from low-Ca boninites, Cape Vogel, Papua New Guinea: evidence for ultramafic primary magma, refractory mantle source and enriched components. *Chem. Geol.* **183**, 287–303 (2002).
15. Portnyagin, M., Almeev, R., Matveev, S. & Holtz, F. Experimental evidence for rapid water exchange between melt inclusions in olivine and host magma. *Earth Planet. Sci. Lett.* **272**, 541–552 (2008).
16. Lahaye, Y., Barnes, S. J., Frick, L. R. & Lambert, D. D. Re-Os isotopic study of komatiitic volcanism and magmatic sulfide formation in the southern Abitibi greenstone belt, Ontario, Canada. *Can. Mineral.* **39**, 473–490 (2001).
17. Evans, K. A., Elburg, M. A. & Kamenetsky, V. Oxidation state of subarc mantle. *Geology* **40**, 783–786 (2012).
18. Kent, A. J. R., Norman, M. D., Hutcheon, I. D. & Stolper, E. M. Assimilation of seawater-derived components in an oceanic volcano: evidence from matrix glasses and glass inclusions from Loihi seamount, Hawaii. *Chem. Geol.* **156**, 299–319 (1999).
19. Gurenko, A. A. & Kamenetsky, V. S. Boron isotopic composition of olivine-hosted melt inclusions from Gorgona komatiites, Colombia: new evidence supporting wet komatiite origin. *Earth Planet. Sci. Lett.* **312**, 201–212 (2011).
20. Ford, C. E., Russell, D. G., Craven, J. A. & Fisk, M. R. Olivine liquid equilibria—temperature, pressure and composition dependence of the crystal liquid cation partition coefficients for Mg, Fe²⁺, Ca and Mn. *J. Petrol.* **24**, 256–266 (1983).
21. Herzberg, C. & O'Hara, M. J. Plume-associated ultramafic magmas of Phanerozoic age. *J. Petrol.* **43**, 1857–1883 (2002).
22. Herzberg, C. & Asimow, P. D. PRIMELT3 MEGA.XLSM software for primary magma calculation: peridotite primary magma MgO contents from the liquidus to the solidus. *Geochem. Geophys. Geosyst.* **16**, 563–578 (2015).
23. Herzberg, C., Condie, K. & Korenaga, J. Thermal history of the Earth and its petrological expression. *Earth Planet. Sci. Lett.* **292**, 79–88 (2010).
24. Herzberg, C. & Gazel, E. Petrological evidence for secular cooling in mantle plumes. *Nature* **458**, 619–622 (2009).
25. Dixon, J. E., Leist, L., Langmuir, C. & Schilling, J. G. Recycled dehydrated lithosphere observed in plume-influenced mid-ocean-ridge basalt. *Nature* **420**, 385–389 (2002).
26. Mibe, K., Orihashi, Y., Nakai, S. i. & Fujii, T. Element partitioning between transition-zone minerals and ultramafic melt under hydrous conditions. *Geophys. Res. Lett.* **33**, L16307 (2006).
27. Roberge, M. *et al.* Is the transition zone a deep reservoir for fluorine? *Earth Planet. Sci. Lett.* **429**, 25–32 (2015).
28. Pearson, D. G. *et al.* Hydrous mantle transition zone indicated by ringwoodite included within diamond. *Nature* **507**, 221–224 (2014).
29. Albarède, F. Volatile accretion history of the terrestrial planets and dynamic implications. *Nature* **461**, 1227–1233 (2009).
30. Falloon, T. J. & Danyushevsky, L. V. Melting of refractory mantle at 1.5, 2 and 2.5 GPa under, anhydrous and H₂O-undersaturated conditions: implications for the petrogenesis of high-Ca boninites and the influence of subduction components on mantle melting. *J. Petrol.* **41**, 257–283 (2000).
31. Ribeiro, J. M. *et al.* Composition of the slab-derived fluids released beneath the Mariana forearc: evidence for shallow dehydration of the subducting plate. *Earth Planet. Sci. Lett.* **418**, 136–148 (2015).
32. Hofmann, A. W. Chemical differentiation of the Earth: the relationship between mantle, continental crust, and oceanic crust. *Earth Planet. Sci. Lett.* **90**, 297–314 (1988).
33. Walter, M. J. Melting of garnet peridotite and the origin of komatiite and depleted lithosphere. *J. Petrol.* **39**, 29–60 (1998).

Supplementary Information is available in the online version of the paper.

Acknowledgements We thank A. Kadik, A. Borisov and A. Kargal'tsev for their assistance in high-temperature experiments, V. Magnin for assistance in maintenance of the EPMA laboratory, U. Westernströer for help with laser-ablation ICP-MS measurements, and V. Kamenetsky for providing sample 41F of the Cape Vogel boninites. The paper benefited greatly from the constructive reviews of C. Herzberg and I. Puchtel and the comments of S. Sobolev. This study was funded by the Russian Science Foundation grant number 14-17-00491 (to A.V.S.). The EPMA facility in ISTERre was established and maintained by funds of the Agence Nationale de la Recherche, France, the Chair of Excellence grant ANR-09-CEXC-003-01 and partly by CNRS and Labex OSUG@2020 (Investissements d'avenir—ANR10 LABX56). A.V.S. acknowledges the support of Institut Universitaire de France and the Deep Carbon Observatory. The costs of SIMS analyses were covered by CRPG (A.A.G.'s internal funds). This is CRPG contribution number 2430.

Author Contributions A.V.S. designed the study, participated in sample collection, data processing and interpretation, and wrote the paper. E.V.A. participated in sample collection, found and prepared melt inclusions in olivines, conducted EPMA analyses and participated in the data processing and interpretation. A.A.G. performed SIMS analyses and participated in data interpretation and writing the paper. N.T.A. led the field work and sample collection, participated in data interpretation and co-authored the paper. V.G.B. managed the EPMA analyses. M.V.P. performed the laser-ablation ICP-MS analyses and participated in data interpretation and writing the paper. D.G.-S. managed the laser-ablation ICP-MS analyses. S.P.K. conducted the heating experiments. All authors discussed the results, problems or methods and participated in preparation of the paper.

Author Information A copy of the Supplementary Information has been submitted to Researchgate (https://www.researchgate.net/profile/Alexander_Sobolev) and GEOROC (<http://georoc.mpch-mainz.gwdg.de/georoc/>) databases. Reprints and permissions information is available at www.nature.com/reprints. The authors declare no competing financial interests. Readers are welcome to comment on the online version of the paper. Correspondence and requests for materials should be addressed to A.V.S. (alexander.sobolev@ujf-grenoble.fr).

METHODS

Samples. The samples are 2.7-billion-year-old komatiites from two outcrops in the Abitibi greenstone belt in Canada: Pyke Hill in Munro Township (M810) and the Alexo flow (M823)^{11,13}. Both samples come from the cumulate B2 zones and contain partly unaltered olivine grains of different size and composition. Sample M810 (Pyke Hill) contains large (1–2 mm) euhedral olivine grains with high-Fo cores (94–94.7 mol% Fo) and less magnesium rims (down to 87 mol% Fo). Sample M823 (Alexo flow) contains smaller (0.5 mm) anhedral olivine grains with zoned cores (92–94 mol% Fo) and Fo-depleted rims (86.5 mol% Fo). The other minerals are skeletal olivine (91–86.7 mol% Fo), equant and skeletal spinel (Cr-number of 60–70), acicular clinopyroxene and altered glass. The cores of olivine grains contain abundant, partly crystallized melt inclusions, which are composed of glass, high-Al clinopyroxene, spinel and gas bubbles (see Extended Data Fig. 1 and Extended Data Table 1).

Analytical methods. To study the compositions of minerals and glasses we used the following in situ analytical techniques: electron probe microanalysis (EPMA), secondary ion mass spectrometry (SIMS) and LA-ICP-MS.

EPMA. Melt inclusions, host olivine and spinel were analysed on a JEOL JXA 8230 microprobe at ISTERre in Grenoble, France. For analyses of olivine we used beam currents from 300 nA to 900 nA and accelerated voltages of 15–25 kV using analytical methods from refs 34 and 35. Melt inclusions were analysed at 12 nA and 15 kV, using GOR-132G (ref. 36) as a standard for major elements and set of international standards for minor and trace elements³⁷. Long counting time (240–300 s) was applied for measurement of trace elements: K, Cl and S. Spinel was analysed at 50 nA and 20 kV using the analytical method from ref. 37. The ZAF correction procedure was applied to correct matrix compositional effects³⁵. **SIMS.** We used secondary ion mass spectrometry (SIMS) to determine the contents of CO₂, H₂O, Cl, F, S and B and the isotopic composition of B in melt inclusions in olivine.

Volatile concentrations in olivine-hosted melt inclusions. The analyses were obtained using the CAMECA IMS 1280 HR and the upgraded CAMECA IMS 1270 E7 ion microprobes at the CRPG in Nancy, France. The inclusion-bearing olivine grains, previously analysed for major elements by EPMA, were carefully re-polished to remove residual carbon coating, with final polishing using 1 µm Al₂O₃ suspension. The grains were then removed from epoxy, remounted by pressing them into indium metal, ultrasonically cleaned and stored at +60 °C. About 12–24 h before analysis, the mount was placed into the sample storage of the ion probe at a pressure of ~10⁻⁸ Torr. A liquid-nitrogen cold trap and a sublimation pump were always used to reduce CO₂ and H₂O background and maintain a pressure of <2 × 10⁻⁹ Torr in the sample chamber. The samples were sputtered with a 0.8–1-nA, 10-kV ¹³³Cs⁺ primary beam focused to a spot of 5–10 µm and then rastered to 10 µm × 10 µm. A field aperture of ~1,000 µm was used to eliminate any secondary ion signal from the spot margins. A mass-resolving power of ~5,000, enough to resolve ¹⁷O from ¹⁶OH and ³⁰Si from ²⁹Si H peaks, was applied. The ¹²C⁻ (counting time 8 s), ¹⁶OH⁻ (6 s), ¹⁹F⁻ (6 s), ²⁷Al⁻ (2 s) and ³⁰Si⁻ (2 s), ³²S⁻ (4 s) and ³⁵Cl⁻ (6 s) ions were counted during 12 cycles after 300 s pre-sputtering, using the axial electron multiplier. A set of reference glasses (ALV981-R23, ALV519-4-1, 30-2, 40-2, VG2 USNM111240, CY84-06-02, CL-DR01-5, KL2-G, ETNA II-6 and ETNA II-7; see Supplementary Table 5) and San Carlos olivine were analysed to create calibration lines, which we used to determine volatile concentrations in the unknown samples. Using the established calibration lines, the accuracy of SIMS analyses (calculated as average relative deviation of the measured values from the reference ones) was estimated to be 6%–24% for CO₂, 6%–20% for H₂O, 4%–10% for F, 2%–6% for S and 8%–24% for Cl (95% confidence level), varying among four separate analytical sessions in March, April and July 2015. The host olivines next to the included glasses were also analysed for volatile concentrations to account for background in each particular grain. The background values calculated assuming zero concentrations of the species in olivine are: 16–21 p.p.m. for CO₂, 60–80 p.p.m. for H₂O, 2–4 p.p.m. for F, 0.3–0.5 p.p.m. for S and 0.7–1.6 p.p.m. for Cl.

Boron contents and isotopic composition of olivine-hosted melt inclusions. Boron contents and isotopic compositions of the homogenized olivine-hosted melt inclusions were analysed using the CAMECA IMS 1280 HR ion microprobe at CRPG. The 10–12-nA 13-kV ¹⁶O⁻ primary beam was focused to 15–20 µm and then rastered to 10 µm × 10 µm, for sample pre-sputtering (10 min) at the beginning of each run and during the analyses. A 400-µm contrast aperture and a 1,000-µm field aperture were used, giving a field of view of approximately 25 µm. Secondary ¹⁰B⁺, ¹¹B⁺ and ²⁸Si⁺⁺ ions were accelerated at 10 kV and analysed at a mass-resolving power of ~2,000, sufficient to resolve ⁹Be H interference on the ¹⁰B peak, ¹⁰B H on the ¹¹B peak and ¹³C H on the ²⁸Si double-charged peak, using a circular focusing mode and a transfer optic of ~150 µm. The energy slit was centred and opened to 50 V. The automatic routine of secondary beam centring in the centre

of field and contrast apertures was used at the beginning of each measurement. High voltage sample control was executed at acquisition begin and then every 20 cycles throughout the acquisition to compensate for possible sample charge usually ranging between 5 and 10 V. Typical ion intensities were 20–60 counts per second (cps) of ¹⁰B⁺, 90–220 cps of ¹¹B⁺ and 70,000–80,000 cps of ²⁸Si⁺⁺ ions. The 1 s.d. internal precision of individual measurements ranged from 3.4% to 5.4%, depending primarily on the boron concentration in the melt inclusions (0.2–0.6 p.p.m. B). The obtained precision was reached after ~2 h of counting (200 cycles, each comprising 12 s, 4 s and 2 s counting time on the ¹⁰B⁺, ¹¹B⁺ and ²⁸Si⁺⁺ peaks, respectively, and 2 s waiting time between each mass change). It matches well the in-run Poisson counting statistics, implying that the instrument was stable.

Instrumental mass fractionation (IMF), expressed as a ratio of the measured to the true values ($\alpha_{\text{IMF}} = R_{\text{measured}}/R_{\text{true}}$), was determined based on the replicate measurements (3–5 times at the beginning and end of the analytical session) of two reference glasses: StHs6/80-G andesite glass (11.6 p.p.m. B, $\delta^{11}\text{B} = -4.4\%$) and GOR132-G basaltic glass (15.6 p.p.m. B, $\delta^{11}\text{B} = +7.1\%$)³⁸. The uncertainty of IMF on ¹¹B/¹⁰B inferred from multiple measurements of the reference glasses was estimated to be ±1.4%, 1 s.d. This is 2–3 times better than the internal precision of individual $\delta^{11}\text{B}$ determinations, mostly due to the low B concentrations in the unknown samples. The $\delta^{11}\text{B}$ values were calculated using ¹¹B/¹⁰B = 4.04558 ± 0.00033 for the NBS 951 standard³⁹.

Boron concentrations were determined using IMF values of ¹¹B⁺/²⁸Si⁺⁺ ratios of the above standards. The precision and accuracy was always better than 4% relative. **LA-ICP-MS.** Trace-element concentrations in melt inclusions and host olivine were analysed by LA-ICP-MS using an Agilent 7500 s quadrupole mass spectrometer coupled with a 193 nm Excimer laser ablation system GeoLas Pro (Coherent) at the Institute of Geosciences of the Christian-Albrecht University of Kiel, Germany. Analyses were performed with 24-µm and 32-µm spots for inclusions and olivine, respectively, 10-Hz pulse frequency, and a laser fluence of 10 J cm⁻². Olivine analyses were performed in three spots around every inclusion, on areas pre-ablated for 3 s to reduce surface contamination. All analyses were performed in a large volume ‘Zürich’ ablation cell. Carrier gas was He (~1 litre per min) with addition of H₂ (0.014 litre per min), which were mixed with Ar (0.85 litre per min) before introduction into spectrometer. Oxide production rate, estimated as ThO⁺/Th⁺, was <0.3%. Analyses were performed in time-resolved mode and included 20 s background measurement followed by 20 s sample ablation and signal measurement. Dwell time was 10 ms for all elements. All spectra were inspected in GLITTER software to define intervals for integration and exclude contamination from the surface. Concentrations were quantified from the measured ion yields normalized to ⁴³Ca for glass and ²⁹Si for olivine. Ca and Si concentrations came from microprobe data, and MPI-DING KL-2G glass was used as a primary standard for all elements³⁶. Other MPI-DING reference glasses (GOR-128G, GOR-132G, BM90/21G) as well as an in-house reference sample of pressed olivine nano-powder tablet (SCOP), were analysed as unknowns. Isobaric interference of ²⁹Si¹⁶O on ⁴⁵Sc was monitored and corrected by using data from Sc-free synthetic quartz, which was measured together with reference glasses every 20 analyses.

Melt inclusions. To eliminate the effects of crystallization of melt inclusions, olivine grains containing inclusions were heated to 1,350–1,400 °C at 1 atm of CO₂-H₂ gas mixture corresponding to the QFM oxygen buffer in a vertical furnace at Vernadsky Institute in Moscow, Russia. Samples were heated for 5 min and then quenched. The olivine grains were then mounted in epoxy and polished to expose melt inclusions on the surfaces. Heated and quenched melt inclusions consist of glass, shrinkage bubbles of low-density gas and spinel (see Extended Data Fig. 1). Melt inclusions that had been originally altered and cracked before or during heating were recognized by very low concentrations of sulfur (below 0.005 wt%) and were filtered out. Measured compositions of glasses in melt inclusions are modified by crystallization of olivine on the walls of cavities, by crystallization of spinel within cavities, and by Fe–Mg exchange between host olivine and included melt⁴⁰. In addition, the segregation of shrinkage bubbles in the inclusions drastically affects the concentration of C in the melt^{41,42}. To reconstruct the original compositions of the trapped melts we applied an algorithm to reverse Fe–Mg exchange between olivine and melt⁴³, based on the olivine melt equilibrium models^{20,21} and the estimated concentrations of FeO in the trapped melt. The FeO contents were estimated as a function of the host olivine composition by modelling the crystallization of the Abitibi komatiite parental melt¹¹ at 250-bar pressure and QFM-1 oxygen fugacity. The compositions and temperatures of trapped melts in equilibrium with host olivine were calculated using Petrolog v.3.1.1.3 software⁴⁴, measured H₂O concentrations, and estimated FeO contents. The concentrations of CO₂ in the inclusions were then corrected for the amount of CO₂ stored in the segregated shrinkage bubbles using estimated bubble volume and density. Bubble volumes were calculated using a relationship between trapping and quenching

temperature⁴¹. Bubble densities were calculated using pressures estimated from the measured concentrations of CO₂ and H₂O in the included glasses and the pressure–volume–temperature properties of CO₂–H₂O mixtures^{45,46}. The estimated concentrations of CO₂ in the melt at the time of entrapment are almost ten times higher than measured ones. They correspond to CO₂–H₂O gas pressures of 150–250 bar⁴⁶.

Geothermometers. To estimate crystallization temperatures, we used partitioning of Fe/Mg and Sc/Y between olivine and melt^{20,21,47} and Al between olivine and spinel⁴⁸. Temperatures obtained from Fe/Mg olivine–melt partitioning were corrected for the effects of measured H₂O contents in the melt using the equation of Falloon and Danyushevsky³⁰. We used this equation rather than those of other models^{49,50} because its calibration includes melts with >15–20 wt% MgO whereas the others are focused in less magnesian melts (≤10 wt% MgO). For Sc/Y thermometry, we used Sc and Y concentrations in olivine and Sc and Y contents of Abitibi komatiites as a function of their MgO concentrations using ref. 51:

$$\text{Sc melt} = 46.3 - 0.733 \times \text{MgO melt}$$

$$\text{Y melt} = 16.4 - 0.326 \times \text{MgO melt}$$

We used the Sc and Y concentrations of rocks rather than melt inclusions to avoid effects of olivine crystallization on inclusion walls on the Sc concentrations in the melt. Calculated Y contents in melts are similar within the error to ones measured in inclusions and corrected for olivine crystallization on the walls.

Olivine–spinel thermometry was applied for olivine containing less than 92 mol% Fo, which crystallize together with spinel. The reported two standard errors of thermometers, including errors in the determination of Y and Al in olivine, are ±30 °C for Sc/Y and Al thermometers^{47,48}, and ±20 °C for the Fe–Mg thermometers^{20,21}.

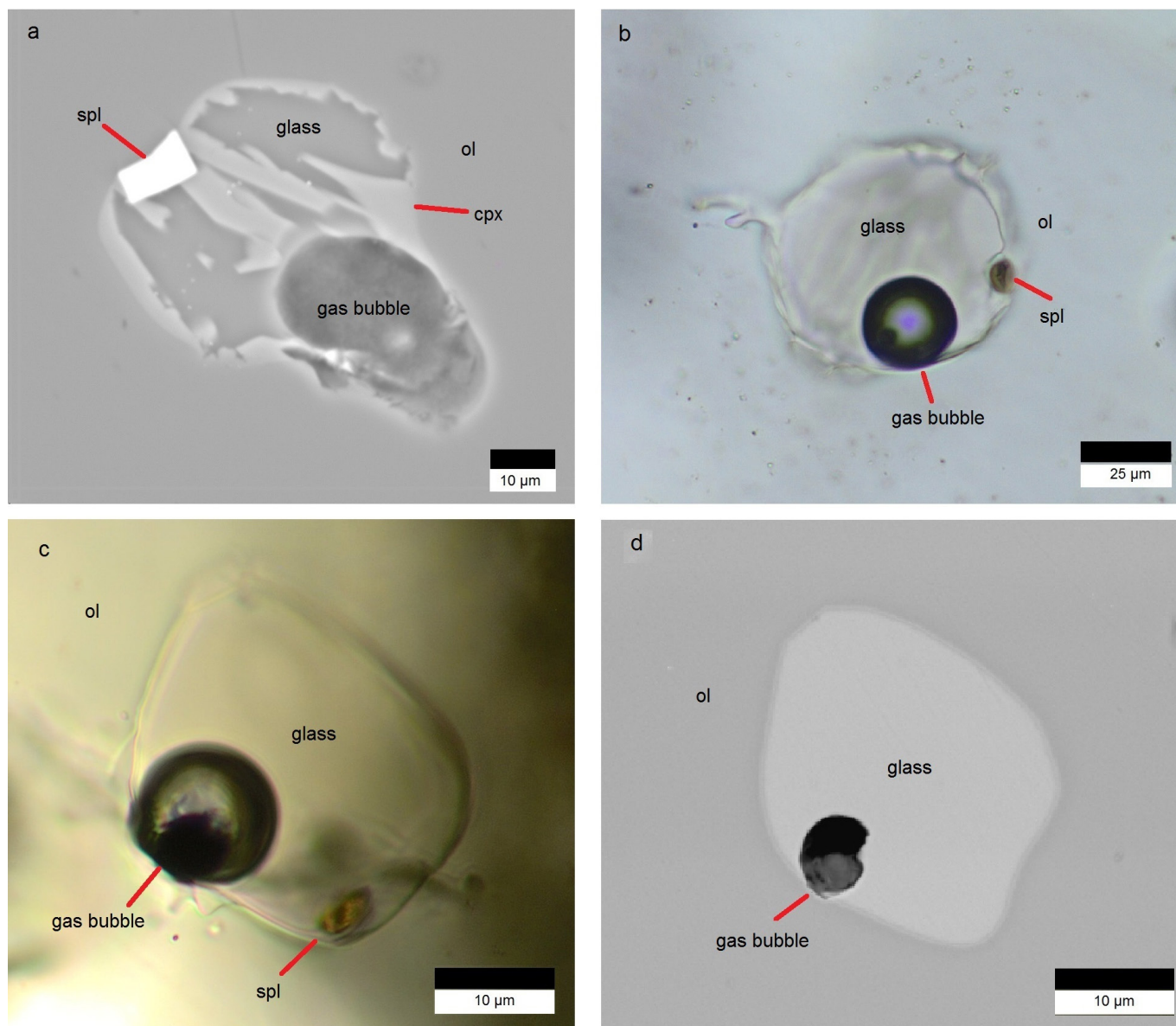
To estimate the oxygen fugacity we used vanadium olivine–melt and V/Sc melt oxybarometers^{47,52}. For that we used V concentrations of olivine and V contents of rocks⁵¹ as a function of their MgO contents:

$$\text{V melt} = 319 - 5.96 \times \text{MgO melt}$$

We also used the average Sc/V ratio of rocks⁵¹. We did not use V concentrations and Sc/V ratios in the included melt because they were affected by crystallization of olivine and spinel in the inclusions.

Contamination. The compositions of trapped melts change with decreasing Fo content of host olivine, but do not follow olivine crystallization paths (Fig. 2). This suggests that contamination accompanies fractional crystallization. Melts trapped in the most Fo-rich olivine in the Pyke Hill sample are least affected by these processes. The most affected is melt inclusion 823-ol31, trapped in the least magnesian olivine in our Alexo flow sample. The amount of olivine crystallized between these two extremes is around 15 wt%. Because of energetic constraints, we assume that the amount of assimilated contaminant is less than the amount of crystallized olivine: between 5 wt% and 15 wt%, and 10 wt% on average. Using this assumption, and known compositions of uncontaminated and contaminated melts, we calculated the composition of the contaminant (Fig. 3a and Extended Data Table 1).

34. Sobolev, A. V. *et al.* The amount of recycled crust in sources of mantle-derived melts. *Science* **316**, 412–417 (2007).
35. Batanova, V. G., Sobolev, A. V. & Kuzmin, D. V. Trace element analysis of olivine: high precision analytical method for JEOL JXA-8230 electron probe microanalyser. *Chem. Geol.* **419**, 149–157 (2015).
36. Jochum, K. P. *et al.* MPI-DING reference glasses for in situ microanalysis: new reference values for element concentrations and isotope ratios. *Geochem. Geophys. Geosyst.* **7**, Q02008 (2006).
37. Batanova, V. G., Belousov, I. A., Savelieva, G. N. & Sobolev, A. V. Consequences of channelized and diffuse melt transport in supra-subduction mantle: evidence from Voykar ophiolite (Polar Urals). *J. Petrol.* **52**, 2483–2521 (2011).
38. Rosner, M. & Meixner, A. Boron isotopic composition and concentration of ten geological reference materials. *Geostand. Geoanal. Res.* **28**, 431–441 (2004).
39. Spivack, A. J. & Edmond, J. M. Determination of boron isotope ratios by thermal ionization mass-spectrometry of the dicesium metaborate cation. *Anal. Chem.* **58**, 31–35 (1986).
40. Sobolev, A. V. & Danyushevsky, L. V. Petrology and geochemistry of boninites from the North termination of the Tonga trench—constraints on the generation conditions of primary high-Ca boninite magmas. *J. Petrol.* **35**, 1183–1211 (1994).
41. Wallace, P. J., Kamenetsky, V. S. & Cervantes, P. Melt inclusion CO₂ contents, pressures of olivine crystallization, and the problem of shrinkage bubbles. *Am. Mineral.* **100**, 787–794 (2015).
42. Mironov, N. *et al.* Quantification of the CO₂ budget and H₂O–CO₂ systematics in subduction-zone magmas through the experimental hydration of melt inclusions in olivine at high H₂O pressure. *Earth Planet. Sci. Lett.* **425**, 1–11 (2015).
43. Danyushevsky, L. V., Sokolov, S. & Falloon, T. J. Melt inclusions in olivine phenocrysts: using diffusive re-equilibration to determine the cooling history of a crystal, with implications for the origin of olivine-phyric volcanic rocks. *J. Petrol.* **43**, 1651–1671 (2002).
44. Danyushevsky, L. V. & Plechov, P. Petrolog3: integrated software for modeling crystallization processes. *Geochem. Geophys. Geosyst.* **12**, Q07021 (2011).
45. Brown, P. E. FLINCOR: a microcomputer program for the reduction and investigation of fluid-inclusion data. *Am. Mineral.* **74**, 1390–1393 (1989).
46. Newman, S. & Lowenstern, J. B. VOLATILECALC: a silicate melt–H₂O–CO₂ solution model written in Visual Basic for Excel. *Comput. Geosci.* **28**, 597–604 (2002).
47. Mallmann, G. & O'Neill, H. S. Calibration of an empirical thermometer and oxybarometer based on the partitioning of Sc, Y and V between olivine and silicate melt. *J. Petrol.* **54**, 933–949 (2013).
48. Coogan, L. A., Saunders, A. D. & Wilson, R. N. Aluminum-in-olivine thermometry of primitive basalts: evidence of an anomalously hot mantle source for large igneous provinces. *Chem. Geol.* **368**, 1–10 (2014).
49. Médard, E. & Grove, T. L. The effect of H₂O on the olivine liquidus of basaltic melts: experiments and thermodynamic models. *Contrib. Mineral. Petrol.* **155**, 417–432 (2008).
50. Almeev, R. R., Holtz, F., Koepke, J., Parat, F. & Botcharnikov, R. E. The effect of H₂O on olivine crystallization in MORB: experimental calibration at 200 MPa. *Am. Mineral.* **92**, 670–674 (2007).
51. Fan, J. & Kerrich, R. Geochemical characteristics of aluminum depleted and undepleted komatiites and HREE-enriched low-Ti tholeiites, Western Abitibi greenstone belt: A heterogeneous mantle plume convergent margin environment. *Geochim. Cosmochim. Acta.* **61**, 4723–4744 (1997).
52. Mallmann, G. & O'Neill, H. S. C. The crystal/melt partitioning of V during mantle melting as a function of oxygen fugacity compared with some other elements (Al, P, Ca, Sc, Ti, Cr, Fe, Ga, Y, Zr and Nb). *J. Petrol.* **50**, 1765–1794 (2009).



Extended Data Figure 1 | Melt inclusions in olivine from Abitibi belt komatiites. **a**, Back-scattered electron image of partly crystallized (unheated) melt inclusion 823-th-ol8 in olivine (ol) of Alexo flow sample M823. The inclusion is composed of glass, quenched clinopyroxene (cpx), spinel (spl) and gas bubble. **b**, Heated and quenched melt inclusion

(810-7-ol1) in olivine from Pyke Hill komatiite sample M810. The inclusion contains glass, gas bubble and spinel. **c**, Heated and quenched melt inclusion (810-9-ol16) in olivine from Pyke Hill komatiite sample M810. The inclusion contains glass, gas bubble and spinel. **d**, Back-scattered electron image of the inclusion in **c**.

Extended Data Table 1 | Representative and average compositions of olivine-hosted melt inclusions and primary melt of the Abitibi belt komatiites

	810-7-	810-7-	810-4-	810-6-	810-7-	823-8-	P. Hill, Fo	Alexo, Fo		PM 1	PM 2	PM avg	Cont.		
	ol1	ol3	ol1	ol20	ol2	ol31	94-94.5	26	93-93.8					26	26
Size, μm	50	20	22	52	30	27	avg	avg	avg	avg	avg	avg	model		
SiO ₂	46.1	45.7	46.0	46.0	46.0	47.0	46.1	0.1	46.6	0.1	45.8	0.1	45.1	0.1	48.4
TiO ₂	0.30	0.30	0.31	0.29	0.28	0.51	0.30	0.01	0.37	0.01	0.29	0.01	0.27	0.01	2.0
Al ₂ O ₃	6.7	7.5	6.8	6.6	6.6	9.0	7.0	0.1	7.6	0.1	6.5	0.1	5.9	0.1	20.5
Fe ₂ O ₃	1.2	1.3	1.3	1.3	1.3	1.2	1.4	0.1	1.2	0.0	1.3	0.0	1.7	0.0	2.5
FeO	10.1	10.0	10.0	10.0	10.0	10.9	9.9	0.1	10.4	0.1	9.6	0.0	8.8	0.0	6.6
MnO	0.10	0.10	0.09	0.09	0.09	0.15	0.09	0.00	0.12	0.00	0.09	0.00	0.12	0.01	0.6
MgO	27.7	27.5	27.8	28.2	28.3	22.8	27.8	0.2	25.7	0.2	29.0	0.1	31.4	0.1	4.7
CaO	6.2	6.4	6.3	6.1	6.0	7.2	6.2	0.1	6.9	0.1	5.9	0.1	5.4	0.1	8.6
Na ₂ O	0.56	0.68	0.55	0.58	0.54	1.05	0.56	0.01	0.66	0.02	0.53	0.01	0.47	0.01	4.7
K ₂ O	0.015	0.031	0.012	0.010	0.012	0.084	0.013	0.001	0.032	0.010	0.012	0.001	0.010	0.001	0.7
P ₂ O ₅	0.020	0.040	0.020	0.023	0.020	0.034	0.020	0.002	0.031	0.005	0.018	0.001	0.016	0.001	0.1
Cr ₂ O ₃	0.24	0.21	0.24	0.25	0.24	0.20	0.24	0.01	0.22	0.01	0.24	0.01	0.22	0.01	0.1
Cl	0.004	0.228	0.005	0.001	0.005	0.054	0.005	0.001	0.020	0.002	0.005	0.001	0.004	0.001	0.5
S	0.032	0.025	0.030	0.023	0.021	0.028	0.026	0.002	0.029	0.002	0.025	0.002	0.022	0.002	0.001
H ₂ Owt%	0.78	0.32	0.51	0.60	0.68		0.66*	0.10	0.17	0.02	0.62	0.06	0.53	0.05	0.06
CO ₂	223		312	116	166		168*	84	222	126	173	74	204	95	61
F	37	18	38	37	32		34*	5	48	3	29	5	22	2	382
S	434	184	467	467	337		413*	70	321	32	348	65	269	42	58
Cl	74	1785	64	67	64		73*	14	214	15	61	12	47	11	12
B				0.18			0.18	0.01	0.46	0.02	0.17	0.01	0.15	0.01	0.02
Sc	26.0	26.2	25.9	25.6	25.6	29.6	25.9	0.2	27.7	0.2	24.5	0.1	22.7	0.1	13
V	154	155	153	150	150	183	153	2	167	2	144	0	130	0	173
Cu	37		25	29	25	72	26	3	44	4	24	3	22	3	422
Rb	0.1		0.2	0.2	0.2	2.3	0.20	0.03	0.62	0.04	0.19	0.02	0.17	0.02	19
Sr	16.2		16.6	15.9	15.0	45.2	16.4	0.6	24.4	1.0	15.5	0.5	14.0	0.5	253
Y	7.4	7.5	7.3	7.2	7.2	9.0	7.3	0.11	8.1	0.10	6.9	0.02	6.2	0.04	10.6
Zr	12.4		12.1	12.7	12.6	30.9	13.1	0.8	18.4	0.3	12.4	0.7	11.2	0.7	154
Nb	0.27		0.28	0.33	0.29	1.3	0.30	0.02	0.51	0.04	0.28	0.01	0.26	0.01	8.6
Ba	2.74		2.46	2.45	2.37	66.4	2.44	0.16	8.01	0.51	2.31	0.13	2.09	0.12	582
La	0.32		0.27	0.28	0.34	1.7	0.30	0.02	0.64	0.02	0.29	0.02	0.26	0.02	12.4
Ce	1.05		0.93	0.99	0.94	4.1	0.98	0.05	1.85	0.07	0.93	0.05	0.84	0.04	27.9
Nd	1.29		1.22	1.23	1.04	3.2	1.20	0.07	1.88	0.11	1.14	0.06	1.03	0.06	17.2
Sm	0.64		0.44	0.69	0.58	1.2	0.55	0.06	0.66	0.06	0.52	0.06	0.47	0.05	5.8
Eu	0.21		0.21	0.25	0.22	0.4	0.22	0.01	0.29	0.02	0.21	0.01	0.19	0.01	1.9
Gd	0.82		0.63	0.86	0.80	1.7	0.89	0.12	1.14	0.07	0.84	0.11	0.76	0.10	6.5
Dy	1.14		1.04	1.43	1.32	2.1	1.29	0.10	1.41	0.11	1.22	0.10	1.11	0.09	6.2
Er	0.77		0.51	0.77	0.62	1.2	0.75	0.08	0.97	0.04	0.71	0.08	0.64	0.07	3.3
Yb	0.91		0.89	0.51	0.71	1.2	0.81	0.08	0.97	0.07	0.77	0.08	0.70	0.07	3.1
Pb					0.09	0.1	0.06	0.02	0.08	0.01	0.06	0.02	0.05	0.02	0.7
T Sc/Y	1482	1497	1542	1517	1530	1442	1505	20	1484	14	1523	20	1523	20	14
T Fe/Mg	1484	1501	1494	1496	1495		1488	10	1482	10	1506	10	1558	10	10
Fo (host)	94.1	94.2	94.2	94.4	94.4	92.4	94.3	0.1	93.5	0.2	94.7		94.7		94.7

All compositions were corrected for host olivine crystallization, Fe–Mg exchange with host olivine and CO₂ loss to the shrinkage gas bubble. See Methods for details. The Fe–Mg olivine–melt partition was calculated after ref. 20, (except PM2 and PM avg, see below). The extremely Cl-rich inclusion (810-7-ol3) and the contaminated inclusion (823-8-ol31) have been excluded from the averages. T Sc/Y and T Fe/Mg are temperatures in degrees Celsius calculated using the models in ref. 47 and ref. 20, respectively (except PM2 and PM avg, see below). PM1, average primary melt for the Pyke Hill calculated using the model in ref. 20; PM2, average primary melt for the Pyke Hill calculated using the model in ref. 21; PM avg, average composition of all primary melts calculated by both models^{20,21}. Cont., composition of the contaminant (see Methods). *Average values calculated for inclusions with diameters larger or equal to 30 μm .